Available online at www.sciencedirect.com
ScienceDirect
Geochimica et Cosmochimica Acta 71 (2007) 3616–3629
Geochimica et Cosmochimica Acta
www.elsevier.com/locate/gca

Searching for parental kimberlite melt

M.G. Kopylova *, S. Matveev [1], M. Raudsepp

Department of Earth & Ocean Sciences, 6339 Stores Road, The University of British Columbia, Vancouver, BC, Canada V6T 1Z4

Received 30 August 2006; accepted in revised form 7 May 2007; available online 23 May 2007

Abstract

Constraining the composition of primitive kimberlite magma is not trivial. This study reconstructs a kimberlite melt composition using vesicular, quenched kimberlite found at the contact of a thin hypabyssal dyke. We examined the 4 mm selvage of the dyke where the most elongate shapes of the smallest calcite laths suggest the strongest undercooling. The analyzed bulk compositions of several 0.09–1.1 mm^2 areas of the kimberlite free from macrocrysts were considered to be representative of the melt. The bulk analyses conducted with a new "chemical point-counting" technique were supplemented by modal estimates, studies of mineral compositions, and FTIR analysis of olivine phenocrysts. The melt was estimated to contain 26–29.5 wt% SiO_2, ~7 wt% of FeO_T, 25.7–28.7 wt% MgO, 11.3–15 wt% CaO, 8.3–11.3 wt% CO_2, and 7.6–9.4 wt% H_2O. Like many other estimates of primitive kimberlite magma, the melt is too magnesian (Mg# = 0.87) to be in equilibrium with the mantle and thus cannot be primary. The observed dyke contact and the chemistry of the melt implies it is highly fluid ($\eta = 10^1$–10^3 Pa s at 1100–1000 °C) and depolymerized (NBO/T = 2.3–3.2), but entrains with 40–50% of olivine crystals increasing its viscosity. The olivine phenocrysts contain 190–350 ppm of water suggesting crystallization from a low SiO_2 magma (a_{SiO_2} below the olivine-orthopyroxene equilibrium) at 30–50 kb. Crystallization continued until the final emplacement at depths of few hundred meters which led to progressively more Ca- and CO_2-rich residual liquids. The melt crystallised phlogopite (6–10%), monticellite (replaced by serpentine, ~10%), calcite rich in Sr, Mg and Fe (19–27%), serpentine (29–31%) and minor amounts of apatite, ulvöspinel-magnetite, picroilmenite and perovskite. The observed content of H_2O can be fully dissolved in the primitive melt at pressures greater than 0.8–1.2 kbar, whereas the amount of primary CO_2 in the kimberlite exceeds CO_2 soluble in the primitive kimberlite melt. A mechanism for retaining CO_2 in the melt may require a separate fluid phase accompanying kimberlite ascent and later dissolution in residual carbonatitic melt. Deep fragmentation of the melt as a result of volatile supersaturation is not inevitable if kimberlite magma has an opportunity to evolve.

1. INTRODUCTION

Knowledge of compositions of kimberlite magma is central to understanding its physical properties, and ultimately, its ascent, fragmentation and emplacement. Reconstructing kimberlite magma compositions, however, is not a trivial task as kimberlites entrain at least 25 vol% of xenolithic component (Scott-Smith, 1996) and only rare textural varieties of coherent kimberlites may have compositions that approximate parental melts.

Estimates of kimberlite melt compositions that appear in the literature were based on various approaches applied to hypabyssal kimberlites. Several attempts at the reconstruction used aphanitic kimberlite as a proxy for a kimberlite magma (Edgar and Charbonneau, 1993; Price et al., 2000). More recently, Le Roex et al. (2003) and Harris et al. (2004) have constrained the compositions of kimberlite magmas by using the trajectories between macrocrystic and aphanitic kimberlite on major element variation diagrams. The authors showed that some aphanitic kimberlites emplaced in late dykes (e.g., the Wesselton aphanitic kimberlite, Edgar and Charbonneau, 1993) are evolved, rich

* Corresponding author. Fax: +1 604 822 6088.
E-mail address: mkopylov@eos.ubc.ca (M.G. Kopylova).
[1] Department of Earth & Atmospheric Sciences, 1-26 Earth Sciences Building, University of Alberta, Edmonton, Alta, Canada TG6 2E3.

0016-7037/$ - see front matter © 2007 Elsevier Ltd. All rights reserved.
doi:10.1016/j.gca.2007.05.009

in Fe and therefore are not representative of primitive kimberlite melt. Another approach was to reconstruct the composition by subtracting a known amount of olivine macrocrysts from analysed hypabyssal samples (Nielsen and Jensen, 2005; Becker and Le Roex, 2006). In many of these studies, kimberlite melts were considered primary even though most of the reconstructed melts were too magnesian to be equilibrated with the mantle.

This work applies a new analytical approach, a "chemical point-counting" technique, to carefully selected samples of hypabyssal kimberlite and constrains the kimberlite melt composition using quenched kimberlite that may be analogous to glassy volcanic rocks traditionally used for reconstruction of parental magmas. The study is based on kimberlite samples in which unusual elongation of groundmass minerals suggests extreme undercooling and rapid crystallization. To address possible criticism that hypabyssal kimberlite in the root facies of pipes may be an agglutinated clastogenic rock that has lost some volatiles (Sparks et al., 2006), our search for kimberlite melts was limited to hypabyssal kimberlite in tabular intrusions with sharp planar contacts.

In searching for quenched textures in kimberlites, several dykes in the Jericho and Gahcho Kue kimberlites have been examined. The best fresh and quenched kimberlite was found among hypabyssal samples from the Jericho kimberlite. From its composition, the study infers melting conditions, contents of volatiles in the magma and olivine phenocrysts, and the sequence and pressure and temperature of crystallization. The reconstructed melt composition is shown not to satisfy the Mg# constrain for a primary magma. In addition, melting conditions of previously reconstructed kimberlite magmas and their properties are re-examined using results from recent petrologic experiments (e.g., Brooker et al., 2001; Brooker, 2006; Keppler, 2003; Giordano and Dingwell, 2003; Gudfinnsson and Presnall, 2005). Finally, the vesicular and amygdaloidal character of the sample supports a study of minerals deposited from the primary kimberlite fluid in comparison to the corresponding magmatic phases.

2. SAMPLES

The Jericho kimberlite (111°28.90′W, 65°59.19′N) is part of a mid-Jurassic (172 ± 2 Ma, Heaman et al., 2003) kimberlite cluster northwest of the main Lac de Gras kimberlite field. The kimberlite, classified as Type Ia, intruded Archean granitoids covered by unknown thicknesses of metaturbidites and Middle Devonian limestones (Cookenboo, 1999). The kimberlite was emplaced in three major successive magmatic phases that formed the intrusion of a 5–20 m thick dyke, two quasi-contemporaneous lobes of Phase 2 volcaniclastic kimberlite, and a lobe of Phase 3 volcaniclastic kimberlite (Cookenboo, 1999) followed by small volume dykes.

Sample JD40 90.2 m represents a late thin (~10 cm) hypabyssal dyke cross-cutting Phase 2 kimberlite in the Jericho pipe at a present depth of 90 m and inferred initial depth of at least 390 m (Cookenboo, 1999). The hypabyssal kimberlite with abundant round vesicles filled with 20–100% carbonate and 0–80% serpentine adjoins the Phase 2 kimberlite along a wavy sharp contact (Fig. 1). Examination of thin sections with a scanning electron microscope revealed an interesting pattern in textures of the hypabyssal kimberlite groundmass minerals. At the contact and no more than 4 mm inside the chilled margin of the kimberlite, the optically cryptocrystalline groundmass is composed of long (~150 μm) laths of carbonate made of smaller isometric patches of calcite and interstitial serpentine (Fig. 1A). Farther from the contact, the laths of calcite become larger and optically discernible (Fig. 1B), and 10 mm away from the contact the texture is replaced by a common texture of the kimberlite groundmass with interstitial anhedral calcite and serpentine. Abundant (10%) round vesicles in the 4–10 mm zone (Fig. 1) are filled by serpentine and rhombic carbonate whose shape indicates growing from the vesicle wall inside an open space. In contrast, volatile segregations further away from the contact resemble regular segregations common in hypabyssal kimberlite; they are not sharply defined, irregular in shape rather than round, and are infilled by a mixture of anhedral calcite and serpentine.

Our analytical work was focused on the 4 mm contact zone of the sample where the most elongate shapes of the smallest calcite laths suggest the strongest undercooling. In two most distant thin sections along the chilled margin of the dyke, we analyzed four different areas of the groundmass (Fig. 2) devoid of macrocrysts. The selected areas contain partly serpentinized olivine and phlogopite phenocrysts set in a matrix of calcite and minor phlogopite laths, interstitial serpentine, euhedral serpentinized monticellite, spinel group minerals, ilmenite, perovskite, apatite, occasional K and Ni sulfides, barite and chlorite (Fig. 2).

3. ANALYTICAL METHODS

The groundmass areas suitable for the bulk quantitative analysis were chosen on a Philips XL30 scanning electron microscope (SEM) (Earth and Ocean Sciences Department, UBC). The areas were analyzed with a fully automated CAMECA SX50 electron microprobe operating in wavelength-dispersion mode (Earth and Ocean Sciences Department, UBC) using an accelerating voltage of 15 kV, beam current of 10 nA, and spot diameter of 30 μm. Peak and background counting times were 20 s and 10 s, respectively. Standards used were synthetic phlogopite (Mg, Si, Al), diopside (Ca), albite (Na), rutile (Ti), synthetic magnesiochromite (Cr), synthetic rhodonite (Mn), synthetic fayalite (Fe), and orthoclase (K). The analyses were done on square or rectangular grids of 100 points covering areas from 0.3 × 0.3 mm (296E-A) to 1.2 × 0.9 mm (296G-C). Analyses for individual points were averaged over the grids (Table 1). The totals for the averaged analyses ranged from 80 to 81 wt% (P_2O_5, CO_2 and H_2O excluded). P_2O_5 was assessed based on weight percentages of apatite calculated from the apatite mode estimated for each individual area of the analysis, and the composition of apatite in the Jericho kimberlite. CO_2 was assessed based on the weight percentage of calcite. This, in turn, was calculated based on the mass balance of Ca, modes of perovskite and apatite, and compositions of perovskite and calcite in each analysed area. H_2O

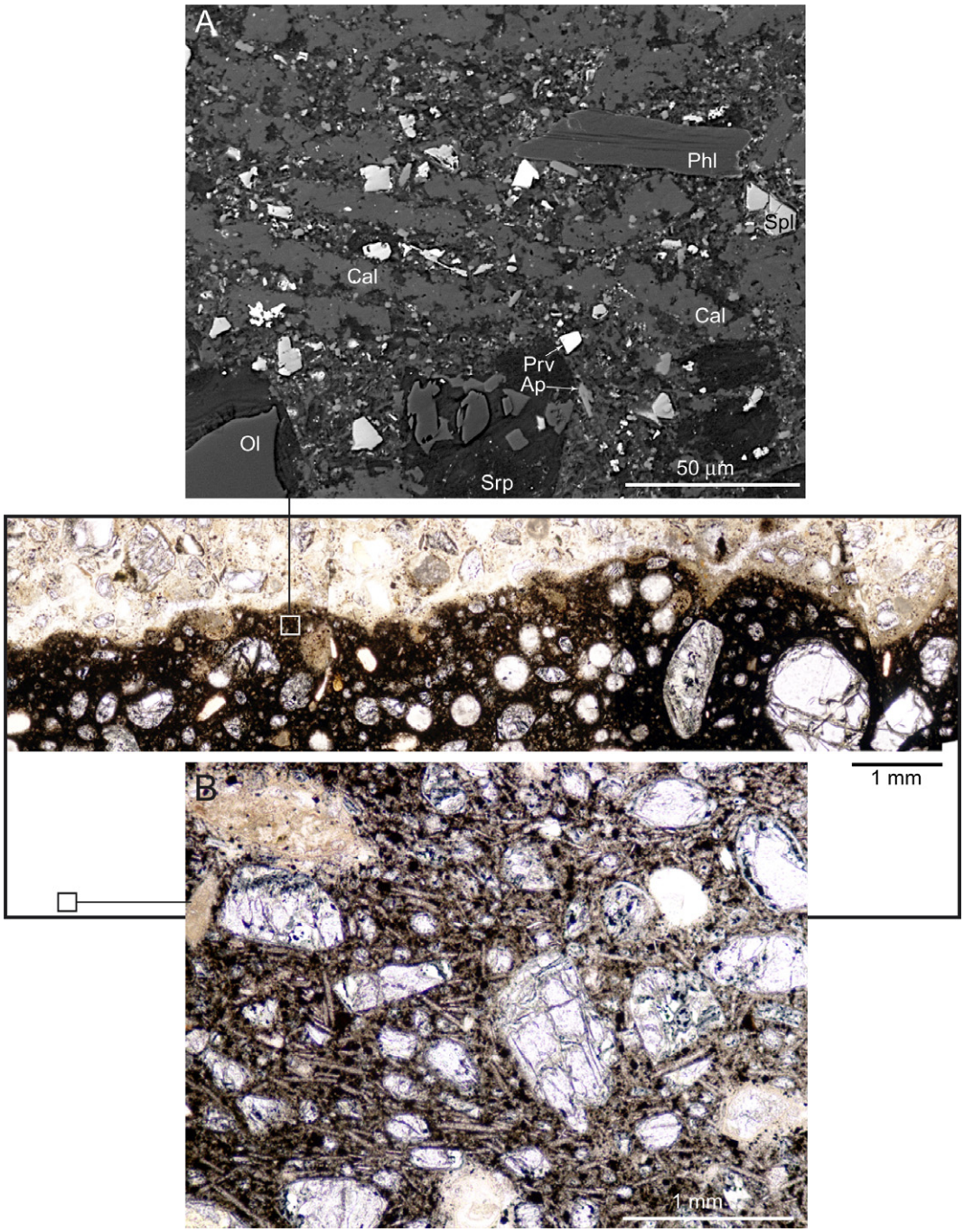

Fig. 1. The contact between quenched hypabyssal kimberlite JD40 90.2m and Phase 2 volcaniclastic kimberlite of the Jericho pipe. Note numerous round vesicles in the hypabyssal dyke. Two insets, (A,B), show enlarged textures of the hypabyssal kimberlite 1–4 mm from the contact (A) and 4–10 mm away from the contact (B).

was computed as the difference between 100% and the analytical totals.

The grid analyses in the four areas (Fig. 2) were supplemented by analyses of all minerals (Tables 2 and 3). Analytical conditions, the precision (2σ) and minimum detection limits (wt%) for these are listed in Electronic Supplementary Table 1.

Proportions of groundmass phases in the areas were assessed using grey-level variation in backscattered electron images via computer-assisted image analysis. Image analysis produces results that are accurate and reproducible to ± 0.3 vol% for some minerals with contrasting grey levels and shapes (oxides, apatite, olivine, serpentine pseudomorphing olivine, and monticellite), but are inaccurate for the rest of the groundmass minerals. In the studied samples, phlogopite shows a range of grey levels, from dark (Ba-free) to light (Ba-rich), thus imitating grey levels in back scattered electron images of lighter calcite to dark serpentine.

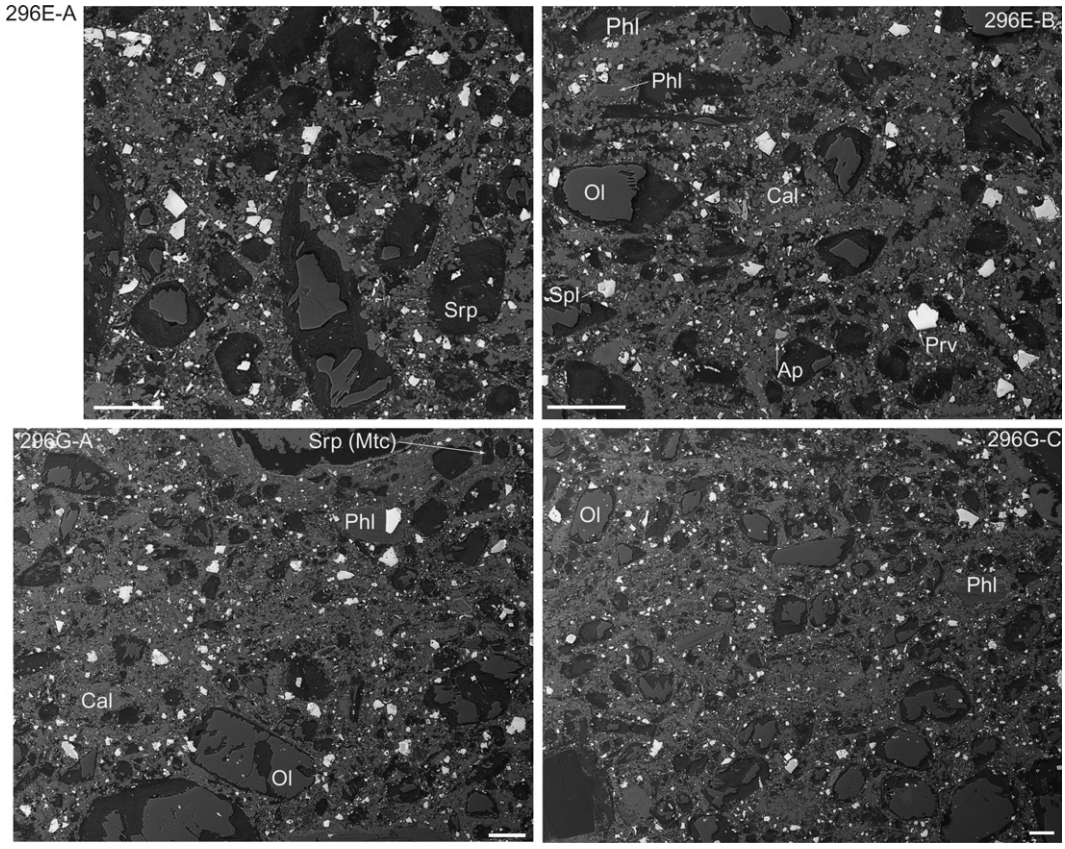

Fig. 2. Back scattered electron images of the groundmass areas in JD40 90.2m used for the EMP grid analysis. The scale bar is 50 μm. The analysed area of 296E-A is 300 by 300 μm covered by 10 × 10 touching points 30 μm each. Areas of 296E-B, 296 G-A and 296 G-C are covered by 10 × 10 non-touching points 30 μm each.

Nevertheless, a reasonable estimate of modal composition for the analysed areas can be made (Table 1). As a check for internal consistency of modal and chemical data, we reconstructed bulk composition on the basis of the modal mineralogy and compared it with the analysed bulk compositions. All elements show a good match, but the analysed compositions were always richer in Al_2O_3 (by up to 0.5 wt%), FeO (by up to 1.8 wt%) and K_2O (by up to 0.8 wt%). This may be ascribed to the presence of Fe and K in accessory sulfides and the residence of Al in phyllosilicates, either as serpentine-septechlorite solid solution, or as serpentine-chlorite mixed layer mineral, or as an interlayer smectite component in serpentine (Stripp et al., 2006). Alternatively, the overestimation of FeO and Al_2O_3 may be inherent to the technique as XRF concentrations of these oxides in a reference specimen (see below) were also lower than the corresponding measured values. The calculated amount of H_2O in the melt has the largest uncertainty among all oxides as some H_2O reside in serpentine pseudomorphing outer rims of olivine phenocrysts (Fig. 2). If the replacement is late, our estimates of H_2O in the melt would be inflated by 2–3.3 wt% (based on the 13–22 vol% pseudomorphed olivine, Table 1).

The grid electron microprobe analysis of the groundmass bulk composition is akin to a petrographic point counting technique and is critically dependent on gaining enough statistics. Since most groundmass mineral grains are only 3–20 μm and each 30 μm analytical spot, on average, covers 10–20 individual grains, each grid analysis averages 1000–2000 mineral compositions. This exceeds the statistics necessary for a representative petrographic modal analysis (Solomon and Green, 1966). Another measure of the robustness of the method is the similarity of the averaged results for the areas. For example, the difference between chemical analyses of SiO_2 derived from various grids is only 2 wt%, and CaO estimates vary by 4 wt% (Table 1). A correlation between the Mg#, Fe content and the presence or absence of olivine phenocrysts is another indication that the averaged analyses of the areas are representative of the mineralogy. Two averaged analyses for the groundmass areas without olivine phenocrysts show higher Fe content and lower Mg# as expected. Accuracy of the new "chemical point-counting" technique was checked against a whole-rock composition of a kimberlite chilled margin specimen analyzed by XRF after removal of olivine crystals (JD69-1, Price et al., 2000; reported also in Table 1). Absolute and relative differences between oxide contents estimated by the new technique and XRF are listed in Electronic Supplementary Table 1 for 2 grid analyses. Compositions calculated from point counts yielded SiO_2 and CaO contents lower than the XRF values by 2.8 wt% and 5.8 wt%, respectively; TiO_2, Al_2O_3, FeO, MgO, and K_2O were

Table 1
Composition and mineralogy of the Jericho parental kimberlite melts in comparison with other estimates of kimberlite melt compositions

Label	Jericho melts (this work)				Literature estimates of kimberlite melts				
	296E-A	296E-B	296G-A	296G-C	Southern Africa			Jericho (Price et al., 2000)	
					Average group I (Becker and Le Roex, 2006)	Kimberley (Le Roex et al., 2003)	Uintjiesberg (Harris et al., 2004)	JD69	JD82
Oxides (wt%)									
SiO_2	29.47	26.64	26.45	28.54	26.15	26–27	24.99	27.00	28.13
TiO_2	1.35	1.38	1.64	1.62	2.58	2.2	3.23	0.5	0.7
Al_2O_3	1.82	1.73	2.33	1.60	2.76	2.2	2.32	1.3	1.6
Cr_2O_3	0.36	0.28	0.38	0.37	0.18		0.22	0.13	0.18
FeO Total	7.36	6.80	6.71	7.38	9.65	8.8	9.16	5.39	6.63
MnO	0.17	0.17	0.17	0.18	0.19		0.19	0.14	0.16
MgO	28.35	26.10	25.77	28.68	25.2	27–26	26.09	22.4	23.1
CaO	11.28	15.08	14.92	12.16	13.26	12.0	14.99	19.4	16.7
Na_2O	0.09	0.12	0.11	0.09	0.16		0.06	0.15	0.19
K_2O	1.46	1.43	1.85	1.19	0.83	1.5	1.87	0.4	0.5
P_2O_5	0.61	0.80	0.94	0.37	2.04		0.30	0.6	0.8
CO_2	8.27	11.35	11.16	9.29	8.19	7.0	8.63	14.01	12.1
H_2O	9.40	8.14	7.57	8.52	7.33	12.3	4.92	7.1	6.7
Total	100.00	100.00	100.00	100.00	98.52	99.0	99.48	99.57	98.63
Mg#	0.874	0.873	0.874	0.875	0.84	0.86	0.846	0.882	0.862
NBO/T	2.77	3.14	3.11	2.93	2.75	2.72–2.57	2.72	3.14	2.79
X CO_2	0.10	0.08	0.07	0.08	0.09	0.07	0.10	0.15	0.13
X H_2O	0.20	0.27	0.27	0.23	0.19	0.29	0.14	0.18	0.18
Mineral modes estimated by image analysis									
Ol fresh	5.1	4.9	8.5	8.8					
Serp after Ol pheno	22.2	15.6	13.4	14.2					
Serp after Mont	9.2	10.2	7.0	7.0					
Spl+Per+Ilm	3.6	3.2	3.9	2.9					
Apatite	1.3	1.7	2.0	0.8					
Phl+Carb+Serp	58.6	64.4	65.2	66.3					
Total	100.0	100.0	100.0	100.0					
Weight% of minerals									
Ol fresh	5.9	5.7	9.9	10.2					
Phlogopite	8.8	5.9	8.9	9.8					
Apatite	1.5	1.9	2.3	0.9					
Total serp	60.9	53.7	48.8	51.2					
Interstitial carb	18.0	28.2	25.9	23.9					
Per	0.9	0.3	0	0.7					
Ilm	2.6	2.0	1.6	1.8					
Spl	1.5	2.3	2.6	1.5					
Total	100.0	100.0	100.0	100.0					

overestimated by 1.2 wt%, 2 wt%, 1.9 wt%, 2.6 wt%, and 0.8 wt%, respectively. Magnesium numbers were lower by 0.01 than those for the XRF analysis.

Olivine phenocrysts in the samples were analysed for water content on a Thermo Nicolet Nexus 470 FTIR spectrometer equipped with the Continuum IR microscope (University of Alberta). During analysis, microscope optics and sample stage area were continuously flushed with a flow of dried air. Such purging significantly reduced spectral noise at 3600 cm^{-1} caused by atmospheric water vapor. FTIR spectra were acquired in transmission mode using unpolarized IR beam at room temperature. The crystallographic orientation of an olivine grain relative to the IR beam was determined after the FTIR analysis using 2nd order Si–O spectral overtone (Jamtveit et al., 2001; Brooker et al., 2001; Matveev et al., 2005). Water concentrations were calculated for olivines analysed with beam oriented parallel to [0 1 0] as described in (Paterson, 1982) and then multiplied by a factor of 3.5 (Bell and Rossman, 2003). For FTIR spectroscopy, 5×10 mm fragment of kimberlite JD40-296F was cut and polished on both sides to produce a 200 μm thick platelet. The IR beam size defined by the aperture of the IR microscope was set to 70×70 μm. FTIR spectra were measured on every optically clear olivine grain of the sample for which areas exposed from both sides of the sample platelet were larger than the beam size.

Table 2
Representative compositions of silicate and carbonate minerals in the groundmass of quenched Jericho kimberlite

Mineral	Serpentine							Olivine	Phlogopite core
Texture	Interstitial					Filling vesicles	Ol & Mtc pseudomorphs		
Av. of						3	3	3	4
SiO_2	41.68	38.93	38.77	40.26	39.00	40.92	40.14	40.58	41.65
TiO_2	N/A	N/A	N/A	N/A	N/A	N/A	N/A	N/A	0.56
Al_2O_3	0.29	0.94	0.36	0.20	0.42	0.40	0.35		10.76
Cr_2O_3	0.09	0.07	0.25		0.03	0.07		0.05	0.21
FeO	2.59	5.91	6.35	7.28	3.13	2.62	6.03	8.41	4.16
MnO	0.08	0.09	0.09	0.12	0.09	0.04	0.09	0.10	0.03
MgO	39.50	36.62	36.86	35.60	38.08	40.27	36.90	49.96	26.24
CaO	0.34	0.79	0.53	0.38	3.00	0.77	0.37	0.05	0.07
Na_2O	0.08	0.07			0.12	0.08			0.08
K_2O	0.18	0.49	0.05	0.04	0.05				10.75
NiO		0.68	0.23	0.06		0.06	0.17	0.38	0.17
BaO		0.18							0.04
Total	84.88	84.78	83.52	83.97	83.96	85.23	84.16	99.58	94.73
Mg#	0.96	0.92	0.91	0.90	0.96	0.97	0.92	0.91	0.92

Mineral	Carbonate								Apatite
	Primary grains in laths and in groundmass interstities						Filling vesicles	Ol pseudomorph	
Texture	Interstitial	Lath	Lath	Lath	Lath	Average primary			
Av. of						5	4		
FeO	0.29	0.42	0.28	0.69	0.64	0.46	0.10	0.22	0.56
MnO	0.08	0.06	0.09	0.07	0.07	0.07	0.11		
MgO	0.41	3.69	0.70	3.21	1.98	2.00	0.15	0.10	0.16
P_2O_5									52.39
CaO	55.01	52.89	54.45	50.94	54.44	53.55	56.79	55.86	41.70
SrO	0.69	0.08	0.51		0.68	0.39	0.26		1.56
La_2O_3	N/A	N/A	N/A	N/A	N/A	N/A	N/A	N/A	0.36
Ce_2O_3	N/A	N/A	N/A	N/A	N/A	N/A	N/A	N/A	0.84
Pr_2O_3	N/A	N/A	N/A	N/A	N/A	N/A	N/A	N/A	0.13
Nd_2O_3	N/A	N/A	N/A	N/A	N/A	N/A	N/A	N/A	0.32
Gd_2O_3	N/A	N/A	N/A	N/A	N/A	N/A	N/A	N/A	0.12
CO_2	43.50	42.85	43.97	45.08	42.20	43.52	42.59	43.82	
Total	100.00	100.00	100.00	100.00	100.00	100.00	100.00	100.00	98.14

All minerals except apatite were analysed in areas used for bulk grid analysis (296E-A, 296 E-B, 296 G-A, 296G-C).
Apatite grains in areas used for bulk grid analysis were too small and were instead analysed in non-quenched samples of the Jericho hypabyssal kimberlite. Blanks—below detection limit, N/A—not analysed, BaO in carbonates are below detection limit but reaches up to 3 wt% in phlogopite rims. CO_2 in carbonates is calculated assuming 100% totals.

4. MINERALOGY

Olivine microphenocrysts have uniform compositions, Fo_{91}, (Table 1) and contain 0.35–0.40 wt% NiO. FTIR spectra of the olivine (Fig. 3) are characterized by the strong OH IR absorption in the wavenumber range between 3650 and 3450 cm^{-1} and suggest the presence of hydroxyl in the tetrahedral sublattice (Matveev et al., 2001; Berry et al., 2005). Based on the hydroxyl peak intensities, water contents of olivine were quantified to be 190–350 ppm, similar to those measured in olivines from other Canadian and South African kimberlites (Matveev, pers. comm.).

The serpentine-group mineral has only traces of Al and a limited solid solution towards the Fe end-member, greenalite. Its Al-poor composition suggests that the mineral is lizardite (Stripp et al., 2006), but structural studies are required to confirm this. Serpentine-group minerals occur in three textural positions: (1) replacing olivine and smaller subhedral grains of possible monticellite, (2) in the groundmass as fine-grained intergrowths with interstitial carbonate and phlogopite, (3) in round vesicles. The three textural varieties of serpentine differ in composition. Serpentine in vesicles is the most Mg-rich (Mg# = 0.97); interstitial serpentines vary significantly in Fe content and occasionally include 3 wt% CaO (Table 2) as a result of sub-microscopic intergrowths with smectite (Zinchuk et al., 2003) or calcite. Serpentine pseudomorphing olivine and monticellite has the most Fe and by Mg# is equal to the precursor olivine.

Carbonate is calcite with minor Mg, Fe, and Sr. Like the serpentine-group minerals, calcites growing in the three

Table 3
Representative compositions of oxide minerals in the groundmass of quenched Jericho kimberlite

Mineral	Spinel group mineral							Perovskite	Ilmenite			
	Groundmass microlites 10–50 μm							Groundmass	Groundmass microlites 50–80 μm			In vesicle
									Zoned grain			
Texture								Core	Rim	Core	Core	
SiO_2	0.06		0.21	0.11	0.06	0.04	0.04		0.09		0.08	
TiO_2	19.60	20.29	20.92	12.76	19.77	18.49	4.61	51.39	52.28	56.27	55.31	51.99
Al_2O_3	3.19	3.52	3.46	3.09	3.01	3.20	2.41					
Cr_2O_3	2.79	1.31	1.25	21.72	3.39	6.51	54.14	0.49	0.23	3.66	3.90	0.07
FeO	53.38	53.65	52.93	45.33	55.16	52.84	26.41	2.01	36.44	20.33	23.24	35.92
MnO	0.89	0.76	0.84	0.64	0.80	0.67	0.35		3.77	0.70	0.54	4.44
MgO	14.79	15.53	15.71	12.91	13.87	14.11	11.40		3.93	16.87	17.16	4.91
CaO	0.27	0.37	0.24	0.23	0.20	0.33	0.20	34.06	0.82	0.54	0.27	0.16
NiO	0.27	0.19	0.19	0.29	0.26	0.29	0.14		0.07	0.23	0.19	
Nb_2O_5		0.09		0.07	0.09			2.91	1.08	0.16	0.08	1.55
Ta_2O_5									0.09			
La_2O_3	N/A	N/A	N/A	N/A	N/A	N/A	N/A	1.33	N/A	N/A	N/A	N/A
Ce_2O_3	N/A	N/A	N/A	N/A	N/A	N/A	N/A	3.31	N/A	N/A	N/A	N/A
Total	95.24	95.72	95.73	97.16	96.61	96.48	99.71	95.69	98.71	98.76	100.68	99.04

All minerals except perovskite were analysed in areas used for bulk grid analysis (296E-A, 296 E-B, 296 G-A, 296G-C).
Perovskite grains in areas used for bulk grid analysis were too small and were instead analysed in non-quenched samples of the Jericho hypabyssal kimberlite. Blanks—below detection limit.

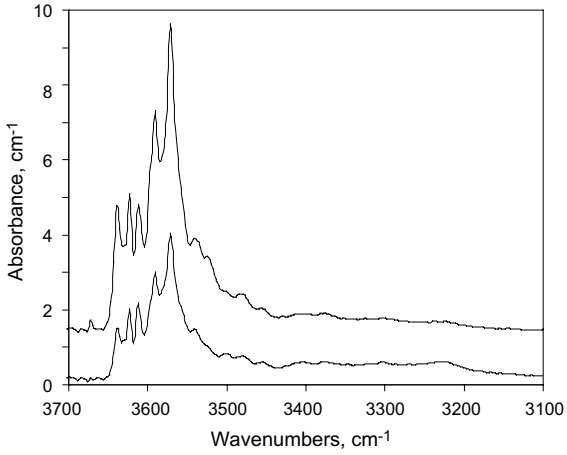

Fig. 3. Representative FTIR spectra of olivine grains in sample JD40 90.2m. The spectra are normalized to 1 cm sample thickness and stacked for clarity.

structural positions have different compositions. Euhedral rhombic calcite does not contain Mg or Fe, but has a measurable amount of Sr (0.26 wt%). Groundmass calcite in laths or interstitally intergrown with serpentine is richer in Mg, Fe, and Sr. Calcite pseudomorphing olivine does not have any Sr (Table 2).

Phlogopite is present as microphenocrysts and as tiny flakes intergrown with groundmass serpentine and calcite. Microphenocrysts are Al-rich (10.5–11.3 wt% Al_2O_3) and Fe-poor (3.8–4.9 wt% FeO_{tot}) and are overgrown by discrete 1–4 μm mantles of barian phlogopite (up to 3 wt% BaO) (Table 2). Groundmass phlogopite is too small to be analysed, but grey levels in the backscattered electron images suggest that it is mostly Ba-poor.

Spinel-group minerals are strongly zoned and only rarely show atoll textures. Most grains are classified as magnesian ulvöspinel-ulvöspinel-magnetites (13–21 wt% TiO_2; 14–16 wt% MgO, 45–52 wt% FeO_{tot}), and occasional cores of titanian magnesiochromite are present (4.6 wt% TiO_2, 54 wt% Cr_2O_3) (Table 3). Ilmenite occurs in the groundmass and in vesicles together with serpentine and calcite. Ilmenite in vesicles has the highest contents of MnO and Nb_2O_5, and is poor in Cr_2O_3. Ilmenite in the groundmass is strongly zoned and shows a decrease in MgO (from 17 to 3 wt%), Cr_2O_3 (from 4 to 0.2 wt%) and a corresponding increase in MnO (from 3.8 to 0.7 wt%) from core to rim (Table 3). Perovskite and apatite failed to produce good analyses because of the small grain sizes. Semi-quantitative analysis showed that by composition these two minerals are similar to those from a "regular", non-quenched samples of the Jericho hypabyssal kimberlite, but perovskite is enriched in Nb_2O_5 (to 7 wt%). For mass balance calculations, compositions of apatite and perovskite from the Jericho Phase 1 hypabyssal kimberlite were used.

5. COMPOSITIONS OF PARENTAL KIMBERLITE MELTS

The bulk composition of the quenched Jericho hypabyssal kimberlite is taken to be representative of a parental kimberlite melt. The melt has 26–29.5 wt% SiO_2, ~7 wt% of FeO_T, 25.7–28.7 wt% MgO, 11.3–15 wt% CaO, 8.3–11.3 wt% CO_2, and 7.6–9.4 wt% H_2O (Table 1). This estimate is close to previously published compositions of kimberlite melts (Price et al., 2000; Le Roex et al., 2003; Harris et al., 2004) for many chemical parameters. Additional

confidence in this result derives from the fact that the estimates done by several various methods agree. Nevertheless, our estimate of the Jericho melt is lower in Ti, Al and Fe and higher in CO_2 than that for primary melts from Southern Africa (Le Roex et al., 2003; Harris et al., 2004). The higher contents of Ti, Al, and Fe in the melt could be a true characteristic of kimberlite magma in Southern Africa, as the Price et al. (2000) estimate for Jericho also shows similar low concentrations of these elements. The major difference between our melt composition and the Price et al. (2000) estimate is lower Mg and Fe and higher Ca and CO_2.

The parental kimberlite melt sampled at the subsurface has evolved during its ascent. For example, the composition of the melt was modified by partial assimilation of peridotite xenoliths resulting in a complete dissolution of orthopyroxene. Instability of orthopyroxene in kimberlite (Shee, 1985; Le Roex et al., 2003; Mitchell, 2006) and other alkaline rocks is well known. Selective resorption and assimilation of orthopyroxene in kimberlites is evident in reaction textures in contacts of mantle peridotites with kimberlites. While olivine in peridotites remains intact, orthopyroxene is entirely serpentinized and "digested" by kimberlites (Shee, 1985). Complete assimilation of orthopyroxene is also evidenced by the low ratio of orthopyroxene to olivine macrocrysts when compared to the orthopyroxene/olivine ratio found in cratonic peridotite (~1:4, Kopylova and Russell, 2000). Reconstruction of the melt composition prior to assimilation of orthopyroxene (Table 4) estimates that this effect leads to a 2 wt% increase of SiO_2, a 0.5 wt% decrease in volatile content and a very slight (0.005) increase in Mg#.

The Jericho primitive kimberlite melt cannot be considered primary as its high Mg# is incompatible with derivation from the mantle. The Jericho melt before assimilation of orthopyroxene had Mg# of 0.86–0.87 which would imply equilibration with Fo_{95} based on an olivine-melt $K_D Fe–Mg = 0.36$ (Herzberg and O'Hara, 2002). The Jericho mantle xenoliths do not have such magnesian olivine in their xenoliths (max Mg# is 0.93, Kopylova et al., 1999a), nor do such Mg-rich olivine phenocrysts crystallize from the melt (Table 2). The Mg# estimate would be even higher if the Fe^{3+} in the melt is accounted for. The discrepancy between Fe and Mg contents of the mantle source and the kimberlite primitive melt cannot be ascribed to a more refractory mantle in the deeper asthenosphere (Kopylova and Russell, 2000) where kimberlites are thought to originate (Mitchell, 1986). The highest Mg-numbers of olivine found as inclusions in diamonds beneath the Slave craton do not exceed 93.6 (Pokhilenko et al., 2004; Davies et al., 2004; Tappert et al., 2005). Similar problems besiege other primitive kimberlite melts with high Mg-numbers that are claimed to be primary (Price et al., 2000; Le Roex et al., 2003).

Table 4
Calculated compositions of evolving kimberlite magma as exemplified by sample 296G-C

Label	Primitive melts		Evolved melts	
	At depth, before assimilation of orthopyroxene	At the subsurface	After crystallization of olivine & monticellite	After crystallization of all groundmass minerals except serpentine & carbonate
Comment	1	2	3	4
Oxides				
SiO_2 (wt%)	26.70	28.54	24.62	22.47
TiO_2	1.73	1.62	2.38	
Al_2O_3	1.57	1.60	2.35	0.54
Cr_2O_3	0.36	0.37	0.55	
FeO total	7.58	7.38	7.07	3.61
MnO	0.18	0.18	0.26	
MgO	28.25	28.68	23.08	22.00
CaO	12.90	12.16	11.12	23.64
Na_2O	0.10	0.09	0.13	
K_2O	1.26	1.19	1.74	0.28
P_2O_5	0.40	0.37	0.55	
CO_2	9.88	9.29	13.64	18.84
H_2O	9.07	8.52	12.51	8.65
Total	99.97	100.00	100.00	100.04
Mg#	0.870	0.875	0.855	
NBO/T	3.09	2.93	2.77	5.19
Mg/Ca (mol)	3.06	3.30	2.91	0.89

1—the composition of the melt was computed by subtraction of 6 vol% orthopyroxene from Jericho melts of Table 1. This number is based on the assessed amount of xenocrystal olivine in kimberlites (25 vol%), and the 78/19 ratio of olivine to orthopyroxene in cratonic peridotite.
2—analysed composition from Table 1.
3—computed melt composition after crystallization of olivine and monticellite phenocrysts (23% olivine and 7% monticellite in sample 296G-C).
4—residual melt calculated as a mixture of interstitial serpentine (32 vol%) and carbonate (24%) as determined for sample 296G-C. Compositions of the minerals are as in Table 2. This estimate assumes that interstitial serpentine and carbonate forms from a residual magma rather than in the subsolidus or from fluids associated with the melt.

6. PARTIAL MELTING OF THE MANTLE AND THE ORIGIN OF KIMBELITE MELT

Compositions of kimberlite provide clues to their origins. For primary magmas, melting conditions can be inferred from experiments on mantle source rocks. The most recent experiments on CO_2-saturated deep melting of peridotite were carried out in the model CMAS–CO_2 system (Gudfinnsson and Presnall, 2005). Despite the fact that the Jericho melt is not primary by the Fe/Mg ratio, proportions of other oxides in the melt may have experienced minor modifications. Therefore, projecting the Jericho melts to the CMAS–CO_2 system may give a reasonable idea on the possible pressures and temperatures of the kimberlite formation. The melt was projected to the model CMAS–CO_2 system by normalizing CaO, MgO, Al_2O_3, SiO_2, and CO_2 to 100% and plotted onto the phase diagram for CO_2-bearing lherzolite (Fig. 4). The high Mg content of the melt limits the pressure at which the melt can coexist with lherzolite to 90 kb. Such deep melting, unfortunately, has not been investigated experimentally and one has to rely on extrapolation of experiments at 30–80 kb (Gudfinnsson and Presnall, 2005) to higher pressures and temperatures. The permissible P–T conditions in the CMAS–CO_2 system are very narrow due to the fact that the low CO_2–CaO melts and low Al_2O_3 melts are mutually exclusive at almost all ranges of P and T. The estimates of 1900–2000 °C, 90–110 kbar obtained for the CMAS–CO_2 system gives the deepest possible conditions of kimberlite formation. The pressures and temperatures are lower for natural compositions where significant amounts of FeO and H_2O are present. The solidus of volatile-free natural peridotite lies 60°C below the comparable solidus in the CMAS–CO_2 system. The CO_2-saturated solidus of peridotite is depressed by 200 °C, and the pressure of the solidus point where carbonate becomes stable is lowered by ~8 kbar (Presnall and Gudfinsson, 2005; Gudfinnsson and Presnall, 2005). Our composition suggest intermediate degrees of saturation with CO_2, thus, the temperature will be lowered by approximately 130 °C and melting conditions for the natural CO_2-bearing lherzolite would be 1770–1870 °C and ~80–100 kbar. Accounting for water content further decreases the solidus temperature, as the water-saturated solidus of carbonate-bearing peridotite is 150 °C lower than the anhydrous solidus (Falloon and Green, 1990). Thus, the Jericho melts are expected to be produced at the maximum T = 1620–1720° and ~80–100 kbar, which is clearly in the petrological asthenosphere (Kopylova et al., 1999b).

These conditions match pressures inferred for primitive kimberlite melts using other experimentally constrained diagrams (Figs. 5 and 6). Ratios of MgO/CaO and SiO_2/Al_2O_3 of Southern African kimberlite melts and the Jericho melt from Price et al. (2000) are compatible with melting at 60–70 kbar, whereas melts from this work suggest melting at 70–90 kbar (Fig. 5). On the MgO–CaO–CO_2 and MgO–CaO–SiO_2 triangles, the melt estimates suggest a somewhat lower range of pressures from 40 to 90 kbar (Fig. 6). The content of CO_2 observed in our Jericho melt can be produced by 0.1–0.7% partial melting of a carbonated mantle source containing 0.02–0.15 wt% of CO_2 in its bulk composition, respectively (Fig. 10 of Gudfinnsson and Presnall, 2005).

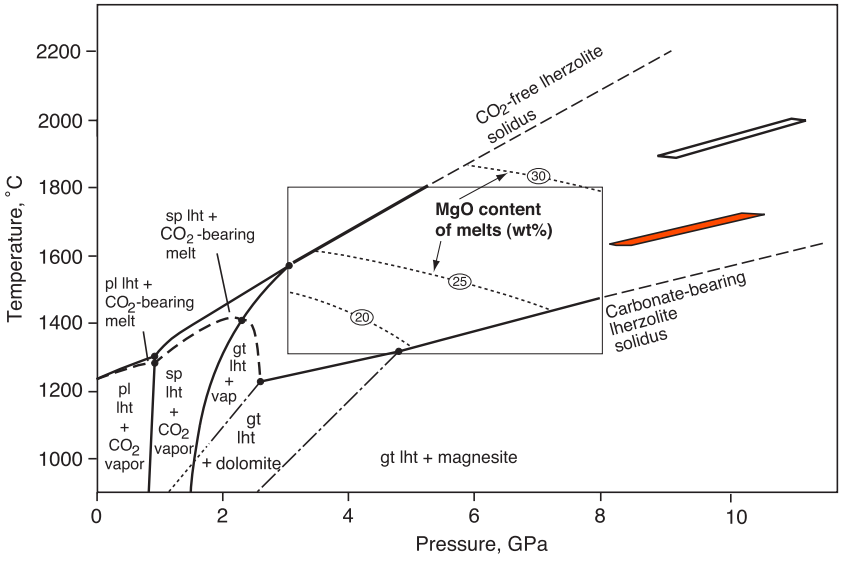

Fig. 4. P–T conditions for generation of CO_2-bearing melts in equilibrium with the garnet lherzolite phase assemblage in the CMAS–CO_2 system. Phase boundaries, solidi, and MgO isopleths (per cent by weight) in the melt are after Gudfinnsson and Presnall (2005). An open rectangle shows a range of pressures and temperatures of experimental work by Gudfinnsson and Presnall (2005), and the phase boundaries extrapolated beyond theses limits are shown as dashed lines. Open P–T field corresponds to inferred conditions where the Jericho primary melt is in equilibrium with the garnet lherzolite in the CMAS–CO_2 system, a black P–T field is the same field corrected for additional components in natural peridotite, mainly Fe and H_2O. To compare Jericho melts with melts in the model system, compositions of the Jericho melts were recalculated to exclude all oxides except CaO, MgO, Al_2O_3, SiO_2, and CO_2 and then normalized to 100%.

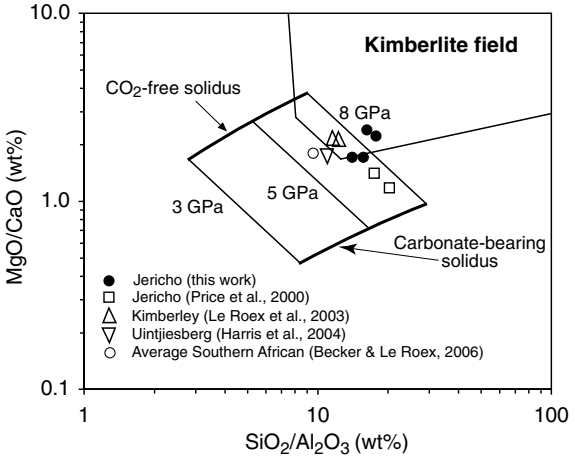

Fig. 5. MgO/CaO vs SiO_2/Al_2O_3 diagram showing compositions of melts generated in equilibrium with garnet lherzolite in the CMAS–CO_2 system (Gudfinnsson and Presnall, 2005). Superimposed on the plot are a field for kimberlite (Rock, 1991) and estimates of primitive kimberlite melts from Jericho (this work and Price et al., 2000) and South Africa (Le Roex et al., 2003; Harris et al., 2004; Becker and Le Roex, 2006).

7. CRYSTALLIZATION AND EVOLUTION OF THE MELT

Several aspects of crystallization and the chemical and thermal evolution of kimberlite magma are elucidated in this study. The largest euhedral phenocrysts and, thus, the first minerals to crystallize from the melt were forsterite and minor phlogopite. FTIR spectra suggest that OH^- in olivine phenocrysts is associated with crystal defects in tetrahedral sublattice (Fig. 3) (Matveev et al., 2001; Berry et al., 2005) and parental magmas had therefore a low a_{SiO_2} and were highly undersaturated in orthopyroxene (Matveev et al., 2001, 2005). Such a result is expected based on the absence of orthopyroxene phenocrysts in kimberlite and is consistent with the inferred composition of the melt. In order to estimate the pressure of olivine crystallization, the observed H_2O content in the Jericho olivine phenocrysts have been compared with experimentally determined water solubilities in forsterite (Fig. 7). The minimum pressure of crystallisation calculated assuming olivine equilibrium with pure aqueous fluid (X H_2O ~1) is between 5 and 15 kbar. Since X H_2O in the primitive kimberlite melt is 0.20–0.27 (Table 1), the pressure necessary to crystallize the observed olivine increases to 30–50 kb (Fig. 7). A more accurate pressure estimate would require the knowledge of a_{H_2O} in kimberlite melt.

The bulk of phenocrystic olivine ceased to crystallize at 30–50 kbar (100–170 km), prior to the development of the groundmass assemblage at the subsurface as the majority of olivine phenocrysts are homogeneous and inclusion-free. Rarely, olivine continues to form during the final emplacement, simultaneously with other groundmass minerals. Such olivine phenocrysts are zoned and in the Jericho kimberlite have a thin Fe-rich outer rim. Numerous microinclusions of late groundmass kimberlite minerals are found mostly in this discrete rim (Kamenetsky, pers. comm.).

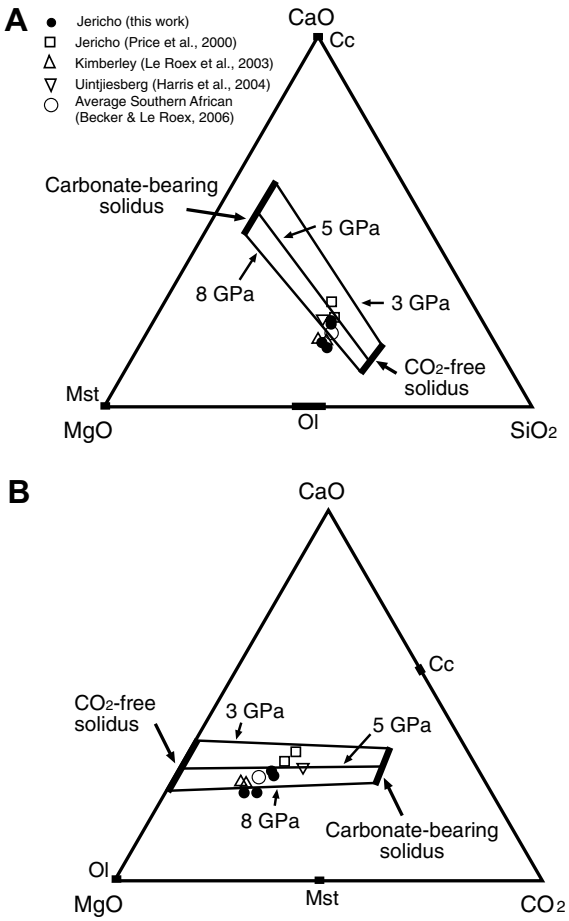

Fig. 6. CaO–MgO–SiO_2 (A) and CaO–MgO–CO_2 (B) plots showing compositions of melts generated in equilibrium with garnet lherzolite in the CMAS–CO_2 system (Gudfinnsson and Presnall, 2005). Superimposed on the plots are estimates of primitive kimberlite melts from Jericho (this work and Price et al., 2000) and South Africa (Le Roex et al., 2003; Harris et al., 2004; Becker and Le Roex, 2006).

Furthermore, 2 kbar (Otto and Wyllie, 1993) and 1 kbar experiments in the CMS–H_2O–CO_2 system (Frantz and Wyllie, 1967 as reviewed in Mitchell, 1986) inevitably find olivine as a liquidus phase in all melts with 5–28% SiO_2.

The reminder of groundmass minerals is thought to crystallize during the final emplacement (Mitchell, 1986, 2006). The first mineral to precipitate during the emplacement is monticellite as it forms euhedral crystals larger than other minerals. Experimental crystallization of melts in the CMS–H_2O–CO_2 system suggest that monticellite may appear on the liquidus of melts with 20–27 wt% SiO_2 at $T > 1100$ °C (2 kb, Otto and Wyllie, 1993). Monticellite may be accompanied by olivine or calcite as evident from the rock texture. The approximate maximum temperature of co-crystallization of forsterite and monticellite is 1050–1100 °C at 2 kbar (Otto and Wyllie, 1993) and 895–975 °C at 1 kbar (Frantz and Wyllie, 1967). Early calcite that occurs in laths is clearly precipitated from melt and not from accompanied vapor as the laths show flow alignment (Fig. 1). Monticellite becomes unstable as the

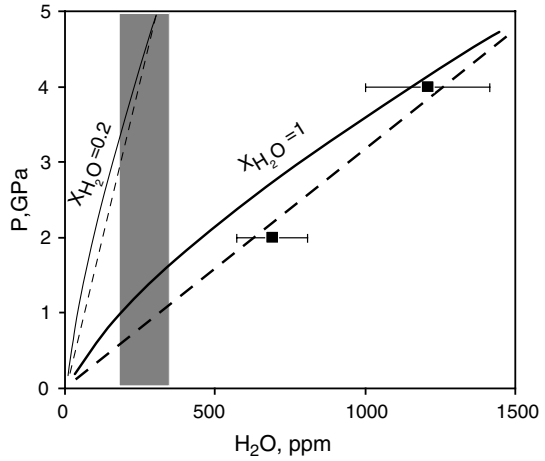

Fig. 7. Comparison of H_2O concentrations measured in olivines from the studied samples with experimentally determined water solubilities in forsteritic olivine. Water concentrations calculated from the FTIR spectra reported in Matveev et al. (2001) are shown as squares and bold dashed line. Bold solid line is a data fit from Kohlstedt et al. (1996) multiplied by the 3.5 coefficient suggested in Bell and Rossman (2003). Thin solid and dashed lines are estimates of water solubilites in olivine equilibrated with a H_2O-rich melt (X $H_2O = 0.2$) using datasets from Kohlstedt et al. (1996) and Matveev et al. (2001), respectively. The melt with X $H_2O = 0.2$ approximates primitive kimberlite melts ($XH_2O = 0.20$–0.27 in this study). Shaded area covers water concentrations in olivines from the examined Jericho samples.

temperature drops to 1000 °C in melt with 18–28% SiO_2 (2 kbar, Otto and Wyllie, 1993) and is replaced by serpentine which may have formed as a result of a reaction between the early phases and the volatile-rich residual magma, or may have precipitated from the fluid that always coexist and evolve in parallel with magmas rich in volatiles. At lower pressures (<1 kbar) monticellite becomes unstable in the CMS–H_2O–CO_2 system below 700–800 °C in the subsolidus (X $CO_2 = 0.05$–0.18; $P = 1$ kbar) and at even higher temperatures in more CO_2-rich compositions in the CaO–MgO–SiO_2–H_2O–CO_2 system (Fig. 29-3, Winter, 2001). High, supersolidus temperatures of monticellite replacement indicate that serpentine pseudomorphing monticellite cannot be subsolidus and may be primary rather than a post-emplacement alteration product. Forsterite is also a metastable phase in the subsolidus below 340–390 °C (at X $CO_2 = 0$–0.2, P = 0.3 kbar, Stripp et al., 2006) in the CMS–H_2O–CO_2 system where it should transform to calcite + serpentine (lizardite).

The parental melt crystallized 15–22% olivine and ~10% monticellite and evolved into a melt enriched in CO_2 (14–17 wt% CO_2) and H_2O (11–16 wt% H_2O), and is poor in Mg, Ca and Si (22–25 wt% SiO_2) (e.g., Analysis 3 in Table 4). The evolved melt crystallised 19–27 vol% calcite, 29–31% serpentine, less than 6% phlogopite, 0.8–2% apatite, and 2.9–3.9% oxide minerals (spinel, ilmenite, and perovskite). Even though serpentine can be a deuteric subsolidus (>300 °C) phase in fresh kimberlites (Mitchell, 2006), the mineralogy of serpentine in the studied samples (see below) attests to its precipitation from the residual melt. Simultaneous crystallization of an oxide mineral, a hydrous mineral and calcite starts at T = 625 °C, 1 kbar in the CMS–H_2O–CO_2 system (Frantz and Wyllie, 1967), which may be relevant to observed co-precipitation of spinel, serpentine and calcite in kimberlite melt. The last minerals to crystallize from the residual melt (Analysis 4 in Table 4) were calcite and serpentine. Co-crystallization of calcite and serpentine from the melt is evident from the rock texture where calcite laths are made of small patches of calcite with minor interstitial serpentine (Fig. 1A). The melt may have crystallized completely at temperatures close to 605 °C (experimental eutectic T in the CMS–H_2O–CO_2 system at 1 kbar, Frantz and Wyllie, 1967) −670 °C (experimental eutectic T in the CMS–H_2O–CO_2 system at 2 kbar, Otto and Wyllie, 1993) depending on pressure.

The mineralogy of serpentine and calcite gives us clues to the crystallization history. The Mg# of serpentine is a reflection of the Mg# of the precursor (e.g., Boyd et al., 1997), as is shown by a good match between Mg# of the olivine and the Mg# of the serpentine, which replaces it. The widely varying Mg# and composition of the interstitial serpentine are thus controlled by its prolonged crystallization from evolving magma progressively enriched in Fe. In a similar manner, groundmass calcite crystallized continuously from hot evolving magma, as suggested by its high and varying contents of Mg, Fe, and Sr. Calcite accepts more Mg and Fe in its solid solution at high temperatures (Anovitz and Essene, 1987), and elevated Sr is considered to be a hallmark of a primary carbonate in kimberlite (Mitchell, 1986; Armstrong et al., 2004; van Straaten et al., 2006). The high Sr contents of calcite filling vesicles attests to its deposition from primary volatiles exsolved from the melt.

Serpentine and calcite in vesicles differ significantly in composition and in the distribution of Mg, Ca, and Fe between these two phases. This is ascribed to their precipitation from the vapor phase exsolved from the melt, a distinctly different bulk composition of the vapor and distribution coefficients of these elements between vapor and melt drastically different from unity (Veksler and Keppler, 2000; Williams-Jones and Heinrich, 2005).

8. VOLATILES IN KIMBERLITE MELT AND CONSTRAINTS ON ITS EMPLACEMENT

Knowing the contents of volatiles in kimberlite melt is important to determine if the melts are saturated with fluids and experience deep degassing and violent emplacement, or are undersaturated and emplace non-explosively.

Solubility of CO_2 in kimberlite melts at low pressure has not been measured directly, but it can be estimated by extrapolating relationships between the melt structure and CO_2 solubility (Brooker et al., 2001) to kimberlites. Key parameters in this extrapolation are the ratio of non-bridging oxygens (NBO) to tetrahedral cations (T) in the melt, Mg content (Brooker et al., 2001) and alkalinity (Brooker, 2006). For CO_2-rich melts, all Fe, ferric and ferrous, act as network-forming cations (Brooker et al., 2001). The calculated NBO/T ratios of kimberlite melts from this work (2.3–3.2, Table 1) display a similar range of NBO/T as

the literature estimations (2.6–3.1; Table 1). Using the NBO/T relationship experimentally produced for non-peralkaline melts with MgO >17 wt% (Brooker, 2006), the NBO/T's of Jericho kimberlite melts suggest CO_2 solubility of 6–8 wt% at 20 kbar and 1400–1600 °C (Fig. 2 of Brooker, 2006). The CO_2 solubility at 1 kbar and 1250–1300 °C decreases to 5–7 wt% (Fig. 3 of Brooker, 2006). This CO_2 content in a saturated peralkaline melt with NBO/T = 2.3–3.2 determines the maximum solubility in a primitive kimberlite melt as it is less alkaline and more magnesian.

A drastic increase in the solubility of CO_2 occurs if kimberlite melt crystallizes at one depth. Early precipitation of Mg-rich silicates makes the melt progressively more Ca-rich and Si-poor (Table 4). Dropping Mg/Ca ratios in evolving kimberlite (from 3.30 to 0.89, Table 4) should enhance CO_2 solubility (Brooker, 2006 and references therein). Experiments on kimberlite melts with varying Mg/Ca ratios, for example, demonstrate that CO_2 solubility increases from 12 to 21 wt% (10 kb, 1700 °C) when MgO/CaO ratio decreases from 1.72 to 0.75 at constant concentrations of other elements (Fig. 4 of Brey and Ryabchikov, 1994). As the Jericho melt evolves (Table 4), it crosses a transition between silicate and carbonate liquids at SiO_2+Al_2O_3 ~20–25% and NBO/T = 3.5 (Brooker, 2006). The CO_2 solubility in the residual ionic carbonate liquid (Analysis 4 in Table 4) is significantly higher because the melt contains isolated molecular CO_2 species, metal-carbonate pairs and approaches pure carbonate melt with 40–44% CO_2. Experimental data (Brooker, 2006) suggest that carbonatitic residual kimberlite melt can accommodate 20 vol% more CO_2 than the primitive kimberlite melt.

Calculated CO_2 concentration in our samples, 8.3–16.7 wt%, reflect the minimum primary CO_2 content in the magma. It is suggested by the accommodation of CO_2 in flow-oriented carbonate laths and by their high Sr content. The CO_2 concentrations of 8.3–16.7 wt% are higher than the CO_2 dissolvable in primitive kimberlite melt at 1–20 kbar, but lower than CO_2 concentrations soluble in the residual kimberlite melt.

Water solubility in kimberlite melt can be evaluated by reference to experimental data on carbonatitic melts. H_2O concentrations calculated for the Jericho primary melt (7.5–9.4 wt% H_2O) are dissolvable in the carbonatitic melt at pressures >0.8–1.2 kbar at T = 900 °C (Keppler, 2003). These estimates give the maximum solubility in the kimberlite melt, as addition of silicate component to carbonatitic melts will decrease the amount of soluble H_2O (Keppler, 2003).

The above solubilities of pure CO_2 and H_2O in the melt serve as the highest possible values limiting the solubilities of these species in the 2-component CO_2+H_2O fluid as a mutual effect of H_2O and CO_2 reduces their saturation content in a combined fluid phase (Papale, 1999; 2006). The influence of H_2O on the CO_2 solubility, although, is more important for kimberlite magma than the reciprocal effect, as CO_2 escapes first during the magma ascent, and this pattern is enhanced under open-system conditions (Papale, 1999). Kimberlite being a magma with high volatile content and high CO_2/H_2O ratio should show an open system behavior (Dixon and Stolper, 1995). Under such conditions, carbon dioxide should be first removed from the melt with negligible loss of water, and during further magma ascent, the water content of the melt should follow the water solubility curve (Dixon and Stolper, 1995). Earlier degassing of CO_2 from the ascending kimberlite magma is supported by petrographic observations on the paucity of carbonates in fragmental kimberlites of the diatreme facies and on the predominance of hydrous deuteric minerals in kimberlites. The extent of the H_2O effect on the CO_2 solubility can be roughly estimated based on data for basalts. The addition of H_2O up to ~8.5 wt% (estimated minimal content of H_2O in the kimberlite magma) produces a 83–29% decrease in the amount of dissolved CO_2 (data for basalt at 1300 K, 0.4–0.6 kb; Fig. 12b of Papale et al., 2006).

Viscosity, a critical parameter controlling magma properties, can also be roughly assessed based on the kimberlite melt compositions through the NBO/T parameter. Extrapolation of experimental data on silicate melts (NBO/T = 0–1.6, Giordano and Dingwell, 2003) to higher NBO/T of kimberlite melts yields viscosities from 10^1 Pa s at 1100 °C (Primitive Melt 2 in Table 4) to 10^3 Pa s at 1000 °C (Evolved Melt 3 in Table 4). Viscosity estimates made with a newer model of volatile-bearing magmas predicts Log η ~3 at T = 1200 °C (Russell et al., 2006). High fluidity of the kimberlite melt devoid of crystal load is evident also in the wavy, irregularly shaped contact of the kimberlite dyke (Fig. 1). In reality, though, the kimberlite melt is emplaced with 40–50 vol% crystals (25% xenocrysts and 15–25% phenocrysts) that should significantly increase η and change the flow regime (Sparks et al., 2006). The above values, therefore, constrain only the low bound on the viscosity of kimberlite melt.

9. CONCLUSIONS

The primitive kimberlite magmas at Jericho assessed by a new methodology of "chemical point counting" are not in equilibrium with the mantle. Selective assimilation of orthopyroxene sourced from entrained cratonic harzburgites is not sufficient to account for the high Mg# of the melt. A search for primary Fe-rich kimberlite melts buffered by $Fo_{91–93}$ and for processes that enrich them in Mg during ascent should be continued. If the primitive kimberlite melts originate in the volatile-saturated peridotitic mantle, they may have been formed as deep as 250–340 km (~80–100 kbar) and have crystallized the bulk of olivine at 30–50 kbar. The melts were thus emplaced as non-Newtonian crystal mush with viscosities limited on the lower side by $\eta = 10^{1-3}$. Crystallization continued until the final emplacement at depths of a few hundred meters and led to progressively more Ca- and CO_2-rich residual liquids. Comparison of CO_2 and H_2O contents with the corresponding solubilities in the 2-component H_2O+CO_2 fluid predicts that the amount of primary CO_2 found at depth of ~400 m in the kimberlite exceeds the amount of CO_2 that can be carried to this depth by primitive kimberlite melt, but roughly matches the amount of H_2O that saturates the primitive kimberlite at this pressure. Residual kimberlite melt that crystallized Mg-silicates, however, is capable of dissolving all observed CO_2 and providing the CO_2 supersaturation

necessary to nucleate bubbles and degas. A supersaturation of 1–3 kbar is needed, for example, for nucleation of CO_2 bubbles in alkaline basaltic melts (Lensky et al., 2006), which are good proxies for kimberlites. Deep fragmentation as a result of volatile supersaturation and 70% vesiculation (e.g., Sparks et al., 2006), therefore, is not inevitable in the kimberlite magma if it has an opportunity to evolve. Geologic observations on shallow inferred depths of explosion for kimberlite pipes (0.5–1 km, Clement and Reid, 1989) and the presence of coherent hypabyssal kimberlites in the subsurface support our conclusion.

One problem associated with the CO_2 budget is that the carbonatitic residual melt forms only at the final stages of emplacement when 40–50% of the melt has crystallized, and effectively stops the melt movement. A process, other than ascent of CO_2 dissolved in the kimberlite melt, should therefore be proposed to transport primary mantle CO_2 into the crust. Such a mechanism, in our opinion, may involve a separate fluid phase accompanying a kimberlite ascent and later dissolution in residual carbonate magma. Experiments on diamond dissolution have determined that common diamond morphologies "require the presence of a H_2O–CO_2 fluid phase through a significant part of kimberlite emplacement history and during the latest stages of kimberlite emplacement" (Fedortchouk et al., in press). This separate fluid phase may exist and entrain together with primitive kimberlite melt at high pressures, but enters residual ionic carbonate liquid left after precipitation of Mg-silicates and oxides at the subsurface. Crystallization of kimberlite should "suck up" free CO_2 enveloping the ascending melt and deposit this CO_2 in carbonate laths precipitating from the melt and as carbonate–serpentine mixtures formed from low-temperature (>300 °C, Mitchell, 2006) deuteric fluids. Experiments reproducing observed crystallization sequences of kimberlites and inferred evolution of the melts at low pressure are needed to test this hypothesis.

ACKNOWLEDGMENTS

The authors thank Canamera Geological Ltd. for samples of the Jericho and Gahcho Kue kimberlite. Lively discussions at the Kimberlite Emplacement Workshop (Saskatoon, 2006) with all participants and especially with R. Brooker and J. Robey helped the first author to develop and test ideas in the paper. A. Le Roux, K. Russell and anonymous reviewers are thanked for constructive comments. Research funding to M.G.K. and M.R. is provided by NSERC.

APPENDIX A. SUPPLEMENTARY DATA

Supplementary data associated with this article can be found, in the online version, at doi:10.1016/j.gca.2007.05.009.

REFERENCES

Anovitz L. M., and Essene E. J. (1987) Phase equilibria in the system $CaCO_3$–$MgCO_3$–$FeCO_3$. *J. Petrol.* **28**(2), 389–414.

Armstrong J. P., Wilson M., Barnett R. L., Nowicki T., and Kjarsgaard B. A. (2004) Mineralogy of primary carbonate-bearing hypabyssal kimberlite, Lac de Gras, Slave Province, Northwest Territories, Canada. *Lithos* **76**, 415–433.

Becker M., and Le Roex A. P. (2006) Geochemistry of South African on- and off-craton, Group I and Group II kimberlites: petrogenesis and source region evolution. *J. Petrol.* **47**(4), 673–703.

Bell D. R., and Rossman G. R. (2003) Hydroxide in olivine: a quantitative determination of the absolute amount and calibration of the IR spectrum. *J. Geoph. Res.* **108**(B2), ECV8-1 - ECV8-9.

Berry A. J., Hermann J., O'Neill H. S. C., and Foran G. J. (2005) Fingerprinting the water site in mantle olivine. *Geology* **33**(11), 869–872.

Boyd F. R., Pokhilenko N. P., Pearson D. G., Mertzman S. A., Sobolev N. V., and Finger L. W. (1997) Composition of the Siberian cratonic mantle: evidence from Udachnaya peridotite xenoliths. *Contrib. Mineral. Petr.* **128**, 228–246.

Brey G. P., and Ryabchikov I. D. (1994) Carbon dioxide in strongly silica undersaturated melts and origin of kimberlite magmas. *Neues Jb. Miner.* **1994**(10), 449–463.

Brooker R. A., Kohn S. C., Holloway J. R., and McMillan P. F. (2001) Structural controls on the solubility of CO_2 in silicate melts. Part I: bulk solubility data. *Chem. Geol.* **174**, 225–239.

Brooker, R. A. (2006) The role of experiments and theory in understanding volatile control on the kimbertlie eruption mechanism. *The Kimberlite Emplacement Workshop*, 8th International Kimberlite Conference, Saskatoon, September 2006. <http://www.venuewest.com/8IKC/files/00%20zContents.pdf> (abstr.).

Clement, C. R., and Reid, A. M. (1989) The origin of kimberlite pipes: an interpretation based on a synthesis of geologic features displayed by southern African occurrences. In *Kimberlites and Related Rock* (eds. J. Ross, A. L. Jaques, J. Ferguson, D. H. Green, S. Y. O'Reilly, R. V. Danchin and A. J. Janse). Spec. Publ. Geol. Soc. Aust. vol. 14 Geological Society of Australia, Perth, pp. 632–646.

Cookenboo H. (1999) Emplacement history of the Jericho (JD-1) kimberlite pipe, Northern Canada. In *Proc. 7th Int. Kimberlite Conf.* (eds. J. J. Gurney and S. R. Richardson). Red Roof Designs, Cape Town, pp. 125–133.

Davies R. M., Griffin W. L., O'Reilly S. Y., and Doyle B. J. (2004) Mineral inclusions and geochemical characteristics of microdiamonds from the DO27, A154, A21, A418, DO18, DD17 and Ranch Lake kimberlites at Lac de Gras, Slave Craton, Canada. *Lithos* **77**(1-4), 39–55.

Dixon J. E., and Stolper E. M. (1995) An experimental study of water and carbon dioxide solubilities in mid-ocean ridge basaltic liquids. Part II: applications to degassing. *J. Petrol.* **36**, 1632–1658.

Edgar A. D., and Charbonneau H. E. (1993) Melting experiments on a SiO_2-poor, CaO-rich aphanitic kimberlite from 5–10 Gpa and their bearing on sources of kimberlite magmas. *Am. Mineral.* **78**(1-2), 132–142.

Falloon T. J., and Green D. H. (1990) Solidus of carbonated fertile peridotite under fluid-saturated conditions. *Geology* **18**(3), 195–199.

Fedortchouk, Y., Canil, D., and Semenets, E. (in press) Mechanisms of diamond oxidation and their bearing on the fluid composition in kimberlite magmas. *Am. Mineral.*

Frantz G. W., and Wyllie P. J. (1967) Experimental studies in the system CaO–MgO–SiO_2–H_2O–CO_2. In *Ultramafic and related rocks* (ed. P. J. Wyllie). John Wiley and Sons, New York, pp. 323–326.

Giordano D., and Dingwell D. B. (2003) Non-arrhenian multicomponent melt viscosity: a model. *Earth Planet. Sci. Lett.* **208**, 337–349.

Gudfinnsson G. H., and Presnall D. C. (2005) Continuous gradations among primary carbonatitic, kimberlitic, melilititic, basaltic, picritic, and komatiitic melts in equilibrium with garnet lherzolite at 3–8 GPa. *J. Petrol.* **46**(8), 1645–1659.

Harris M., Le Roex A., and Class C. (2004) Geochemistry of the Uintjiesberg kimberlite, South Africa: petrogenesis of an off-craton, Group I kimberlite. *Lithos* **74**(3–4), 149–165.

Heaman L. M., Kjarsgaard B., and Creaser R. A. (2003) The timing of kimberlite magmatism and implications for diamond exploration: a global perspective. *Lithos* **71**(2–4), 153–184.

Herzberg C., and O'Hara M. J. (2002) Plume-associated ultramafic magmas of Phanerozoic age. *J. Petrol.* **43**(10), 1857–1883.

Jamtveit B., Brooker R., Brooks K., Larsen L. M., and Pedersen T. (2001) The water content of olivines from the North Atlantic Volcanic Province. *Earth Planet. Sci. Lett.* **186**(5772), 401–415.

Keppler H. (2003) Water solubility in carbonatite melts. *Am. Mineral.* **88**, 1822–1824.

Kohlstedt D. L., Keppler H., and Rubie D. C. (1996) Solubility of water in the alpha, beta and gamma phases of $(Mg,Fe)_2SiO_4$. *Contrib. Miner. Petr.* **123**, 345–357.

Kopylova M. G., Russell J. K., and Cookenboo H. (1999a) Petrology of peridotite and pyroxenite xenoliths from the Jericho kimberlite: implications for the thermal state of the mantle beneath the Slave craton, Northern Canada. *J. Petrol.* **40**(1), 79–104.

Kopylova, M. G., Russell, J. K., and Cookenboo, H. (1999b) Mapping the lithosphere beneath the North Central Slave Craton. In *Proc. 7th Int. Kimberlite Conference*, (eds. J. J. Gurney and S. R. Richardson). Red Roof Designs, Cape Town, pp. 468–479.

Kopylova M. G., and Russell J. K. (2000) Chemical Stratification of cratonic lithosphere: constraints from the Northern Slave craton, Canada. *Earth Planet. Sci. Lett.* **181**, 71–87.

Le Roex A. P., Bell D. R., and Davis P. (2003) Petrogenesis of Group I kimberlites from Kimberley, South Africa: evidence from bulk-rock geochemistry. *J. Petrol.* **44**(12), 2261–2286.

Lensky N. G., Niebo R. W., Holloway J. R., Lyakhovsky V., and Navon O. (2006) Bubble nucleation as a trigger for xenolith entrapment in mantle melts. *Earth Planet. Sci. Lett.* **245**, 278–288.

Matveev S., O'Neill H. S. C., Ballhaus C., Taylor W. R., and Green D. H. (2001) Effect of silica activity on OH^- IR spectra of olivine: implications for low-aSiO_2 mantle metasomatism. *J. Petrol.* **42**(4), 721–729.

Matveev S., Portnyagin M., Ballhaus C., Brooker R., and Geiger C. A. (2005) FTIR spectrum of phenocryst olivine as an indicator of silica saturation in magmas. *J. Petrol.* **46**, 603–614.

Mitchell R. H. (1986) *Kimberlites: Mineralogy, Geochemistry, and Petrology*. Plenum Press, New York, 442 pp.

Mitchell, R. H. (2006) Petrology of hypabyssal kimberlites. *The Kimberlite Emplacement Workshop*, 8th International Kimberlite Conference, Saskatoon, September 2006. <http://www.venuewest.com/8IKC/files/00%20zContents.pdf> (abstr.).

Nielsen, T. F. D., and Jensen, S. M. (2005) The Majuagaa calcite-kimberlite dyke, Maniitsoq, southern West Greenland. *Danmarks og Gronlands Geologiske Undersogelse Rapport* **43**, 59 pp.

Otto J. W., and Wyllie P. J. (1993) Relationships between silicate melts and carbonate-precipitating melts in CaO–MgO–SiO_2–CO_2–H_2O at 2 kbar. *Miner. Petrol.* **48**, 343–365.

Papale P. (1999) Modeling of the solubility of a two-component H_2O+CO_2 fluid in silicate liquids. *Am. Mineral.* **84**, 477–492.

Papale P., Moretti R., and Barbato D. (2006) The compositional dependence of the saturation surface of H_2O+CO_2 fluids in silicate melts. *Chem. Geol.* **229**(1–3), 78–95.

Paterson M. (1982) The determination of hydroxyl by infrared absorption in quartz, silicate glasses and similar materials. *Bull. Mineral.* **105**, 20–29.

Pokhilenko N. P., Sobolev N. V., Reutskya V. N., Hallb A. E., and Taylor L. A. (2004) Crystalline inclusions and C isotope ratios in diamonds from the Snap Lake/King Lake kimberlite dyke system: evidence of ultradeep and enriched lithospheric mantle. *Lithos* **77**(1–4), 57–67.

Presnall, D. C., and Gudfinsson, G. H. (2005) Carbonate-rich melts in the oceanic low-velocity zone and deep mantle. In *Plates, Plumes and Paradigms*. (eds. G. R. Foulger, J. H. Natland, D. C. Presnall and D. L. Andersen). Geol. Soc. Am. Spec. Pap. 388, 207–216.

Price S. E., Russell J. K., and Kopylova M. G. (2000) Primitive magma from the Jericho Pipe, NWT, Canada: constraints on primary kimberlite melt chemistry. *J. Petrol.* **41**(6), 789–808.

Rock N. M. S. (1991) *Lamprophyres*. Blackie, New York, 390 pp.

Russell, J. K., Giordano, D., Kopylova, M., and Moss, S. (2006) Transport properties of kimberlite melt, *The Kimberlite Emplacement Workshop*, 8th International Kimberlite Conference, Saskatoon, September 2006. <http://www.venuewest.com/8IKC/files/00%20zContents.pdf> (abstr.).

Scott-Smith, B. (1996) Kimberlites. In: *Undersaturated Alkaline Rocks: Mineralogy, Petrogenesis, and Economic Potential*. (ed. R. H. Mitchell). MAC, Short Course Volume, Winnipeg 24: 217–244.

Shee, S. R. (1985) The petrogenesis of the Wesselton Mine kimberlite, Kimberley, Cap province, R.S.A. PhD Thesis, University of Cape Town.

Solomon M., and Green R. (1966) A chart for designing modal analysis by point counting. *Geologische Rundschau* **55**(3), 844–848.

Sparks R. S. J., Baker L., Brown R. J., Field M., Schumacher J., Stripp G., and Walters A. (2006) Dynamical constraints on kimberlite volcanism. *J. Volc. Geoth. Res.* **155**, 18–48.

Stripp G. R., Field M., Schumacher J. C., Sparks R. S. J., and Cressey G. (2006) Post-emplacement serpentinization and related hydrothermal metamorphism in a kimberlite from Venetia, South Africa. *J. Metam. Geol.* **24**, 515–534.

Tappert R. S. T., Harris J. W., Shimizu N., and Brey G. P. (2005) Mineral inclusions in diamonds from the Panda Kimberlite, Slave Province, Canada. *Eur. J. Mineral.* **17**(3), 423–440.

van Straaten, B., Kopylova, M., Russell, K., Webb, K., and Scott Smith, B. (2006) Victor North pyroclastic kimberlite, Ontario: resourse vs non-resource distinguished. *Kimberlite Emplacement Workshop*, September 2006, Saskatoon. <http://www.venuewest.com/8IKC/files/00%20zContents.pdf> (abstr.).

Veksler I. A., and Keppler H. (2000) Partitioning of Mg, Ca, and Na between carbonatitie melt and hydrous fluid at 0.1–0.2 GPa. *Contrib. Mineral. Petr.* **138**, 27–34.

Williams-Jones A. E., and Heinrich C. (2005) Vapor transport of metals and the formation of magmatic-hydrothermal ore deposits. *Econ. Geol.* **100**, 1287–1312.

Winter J. D. (2001) *An Introduction to Igneous and Metamorphic Petrology*. Prentice Hall, Upper Saddle River, New Jersey, 697 pp.

Zinchuk N. N., Kotel'nikov D. D., and Gorshkov A. I. (2003) Identification and genesis of the mixed-layer lizardite-saponite phase in a kimberlite pipe, South Africa. *Lithol. Miner. Res.* **38**, 78–81.

Associate editor: J. Kelly Russell